Weierstraß-Institut
für Angewandte Analysis und Stochastik
Leibniz-Institut im Forschungsverbund Berlin e. V.

Preprint ISSN 2198-5855

Inverse modeling of thin layer flow cells for detection of solubility, transport and reaction coefficients from experimental data

Jürgen Fuhrmann[1], Alexander Linke[1] , Christian Merdon[1] , Felix Neumann[1] ,

Timo Streckenbach[1] , Helmut Baltruschat [2] , Mehdi Khodayari[2]

submitted: October 12, 2015

[1] Weierstrass Institute
Mohrenstr. 39
10117 Berlin
Germany
email: Jürgen.Fuhrmann@wias-berlin.de
Alexander.Linke@wias-berlin.de
Christian.Merdon@wias-berlin.de
Felix.Neumann@wias-berlin.de
Timo.Streckenbach@wias-berlin.de

[2] Universität Bonn
Römerstr. 164
53117 Bonn
Germany
email: baltruschat@uni-bonn.de
khodayari@uni-bonn.de

No. 2161
Berlin 2015

2010 *Mathematics Subject Classification.* 76D07, 65N30, 65N08.

Key words and phrases. Stokes equations, mixed finite elements, convection diffusion equation„ finite volume method, electrochemical flow cell.

Edited by
Weierstraß-Institut für Angewandte Analysis und Stochastik (WIAS)
Leibniz-Institut im Forschungsverbund Berlin e. V.
Mohrenstraße 39
10117 Berlin
Germany

Fax: +49 30 20372-303
E-Mail: preprint@wias-berlin.de
World Wide Web: http://www.wias-berlin.de/

Abstract. Thin layer flow cells are used in electrochemical research as experimental devices which allow to perform investigations of electrocatalytic surface reactions under controlled conditions using reasonably small electrolyte volumes. The paper introduces a general approach to simulate the complete cell using accurate numerical simulation of the coupled flow, transport and reaction processes in a flow cell. The approach is based on a mass conservative coupling of a divergence-free finite element method for fluid flow and a stable finite volume method for mass transport. It allows to perform stable and efficient forward simulations that comply with the physical bounds namely mass conservation and maximum principles for the involved species. In this context, several recent approaches to obtain divergence-free velocities from finite element simulations are discussed. In order to perform parameter identification, the forward simulation method is coupled to standard optimization tools. After an assessment of the inverse modeling approach using known real-istic data, first results of the identification of solubility and transport data for O2 dissolved in organic electrolytes are presented. A plausibility study for a more complex situation with surface reactions concludes the paper and shows possible extensions of the scope of the presented numerical tools.

1. Introduction

Thin layer flow cells provide a controlled environment for the investigation of electrocatalytic surface reactions [JMB99, Bal04]. Coupled with a mass spectrometer, they allow to perform simultaneous quantitative measurements of Faradaic currents and flows of reaction products. The interpretation of this detailed information relies on mathematical models of the experimental process and their approximate solution. Depending on the particular experimental situation, these models may combine the description by partial differential equations of fluid flow, multiple species solute transport, potential distribution and Faradaic reactions [NTA12]. In the limit of high reaction rates (depending on the applied potential), a simplified single species transport model coupled to fluid flow in the case of simple geometrical situations allows to apply asymptotic techniques. This approach is a classical tool for the quantitative interpretation of limiting current experiments for high fluid velocities [Lev62]. It provides as well a valuable possibility to benchmark the solution methods for the more complex case [FZH+08]. Simplified geometrical situations allow as well to apply well known finite difference based numerical solution approaches [AKS10, CLW14]. These are able to handle a larger set of coupled processes in a model. Finite element based numerical software promises to be a tool which allows for comparably easy implementation of complex model sets in more general geometries [AES14].

However, for standard finite element based numerical ansatzes for species transport equations, a number of fundamental questions is still not satisfactorily answered [JK07]. These in particular concern the qualitative properties of discretized solutions, prominent amongst

them positivity of concentrations, guaranteed nonoscillatory behaviour, observance of natural physical bounds [ACF+11].

One of the main difficulties in the finite element discretisation of the Navier–Stokes equations is strict observation of the divergence constraint which is inherently connected to the conservation of mass and the preservation of physical bounds in the coupled mass transport equation. Any perturbation of the divergence constraint $\nabla \cdot \vec{u} = 0$ can lead to a violation of positivity and unphysical overshoots for the concentration c.

These open questions motivate the search for methods which allow for guaranteed good qualitative performance in this respect in the case of general geometries. The present paper gives an overview of some new ansatzes in this direction, and discusses their merits in the particular application of thin layer flow cells.

A possible approach to address these questions was based on a exactly divergence-free finite element method coupled to an unconditionally stable upwind Delaunay-Voronoi finite volume method [FLLB09, FLL11]. This approach was successfully used to determine the limiting current behaviour of a thin-layer flow cell [FLLB09]. The exact conservation of the divergence constraint was based on the Scott–Vogelius finite element method. However, this method is very expensive, especially in three space dimensions.

In this paper we suggest other techniques to ensure the preservation of the divergence constraint, and thus mass conservation. One quite plain but universal approach is a divergence-free postprocessing of the discrete solution by projection into a divergence-free subspace. This approach works with any out-of-the-box finite element method, even with very cheap ones like the mini finite element method.

However, this approach cannot heal intrinsic errors of the finite element method that come from the usage of non-divergence-free test functions, i.e. there is an additional term ($C_2 = 1$) in the a priori error estimate [GR86, BF91]

$$\|\nabla_h(\vec{u} - \vec{u}_h)\|_{L^2(\Omega)} \leq C_1 \inf_{\vec{w}_h \in V_h} \|\nabla_h(\vec{u} - \vec{w}_h)\|_{L^2(\Omega)} + \frac{C_2}{\eta} \inf_{q_h \in Q_h} \|p - q_h\|_{L^2(\Omega)} \,. \tag{1.1}$$

If the second term on the right-hand side is large compared to the first one, the discrete solution can deteriorate, even for very simple real-world situations [LM14]. In this case also the projected velocity cannot be expected any better. In other words, the a posteriori projection approach ensures mass conservation but still lacks accuracy in case of large or complicated pressures. To avoid this error term, some finite element methods can be modified in the spirit of [Lin14]. Here, the only discretely divergence-free test functions (see equation (4.2)) are projected onto exactly divergence-free test functions. In some sense the a posteriori projection idea is performed at an earlier stage. This has the advantage, that due to the locality of the basis functions, their reconstruction is also local and cheap. Moreover, since the reconstruction operator is linear, this also results in a global reconstruction operator for free. Hence, this ansatz has the capability to improve the quality of the discrete solution in case of large pressures ($C_2 = 0$ in (1.1)) and offers a divergence-free reconstruction of the discrete solution such that the coupling to solute transport proposed in [FLL11] is mass conservative and ensures positivity of concentrations and the absence of unphysical overshoots.

The remaining parts of the paper are structured as follows. Section 2 describes the experimental setup. Section 3 introduces the mathematical model. Section 4 elaborates on the numerical tools for the discretisation. Section 5 presents ideas and modifications that ensure a mass conservative coupling. Section 6 describes the parameter identification algorithm that fits the simulation data to experimental data. Section 7 reports on the numerical results. Section 8 concludes with an example where the model is extended to the simulation of CV measurements and the detection of kinetic constants.

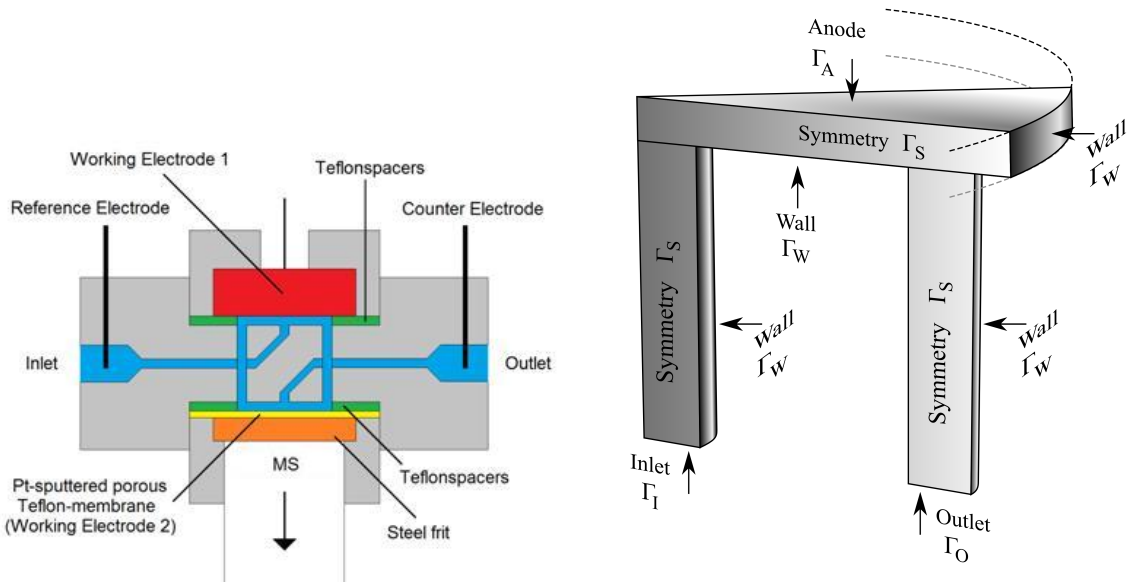

FIGURE 2.1. Schematic view on the thin-layer flowcell (left) and the reduced computational domain Ω with boundary regions (right).

2. Experimental Setup

This section explains the composition of the dual thin-layer flow cell depicted in Figure 2.1[left] and the experimental setup.

The cell consists of two working chambers defined by a Teflon spacer of $6mm$ inner diameter and about $75\mu m \pm 25\mu m$ thickness. The electrolyte passes from the inlet through an $1mm$ thick capillary into the electrode chamber (where the electrode is replaced by a Kel-F dummy for this work). Then, via six centro-symmetric capillaries of radius $0.25mm$, the electrolyte enters the lower compartment. Here a hydrophobic volatile-permeable membrane separates the electrolyte from the vacuum that leads to the mass spectrometer (MS). Only dissolved gas (or the vapor of volatile species) can penetrate the membrane and enter the mass spectrometer. Then the electrolyte leaves the cell through the outlet. A constant flow through the cell with a uniform and well-reproducible flow rate is provided by an Alladdin programmable syringe pump at the outlet [Kho15].

3. Mathematical Model

This section explains the mathematical model for the species flow through the thin-layer flow cell depicted in Figure 2.1[left] and the concept of weak solutions.

3.1. **Governing Equations.** Let $\Omega \subset \mathbb{R}^d$ denote a simply connected Lipschitz domain of dimension $d \in \{2, 3\}$. For a given velocity inflow profile $u_I \in L^2(\Gamma_I; \mathbb{R}^d)$ and right-hand side $\vec{f} \in L^2(\Omega)^d$, the stationary, incompressible Stokes equations establish a velocity field $\vec{u}$ and a pressure p with

$$\nabla p - \eta \Delta \vec{u} = \vec{f}, \quad \nabla \cdot \vec{u} = 0 \quad \text{and} \quad \vec{u} = \vec{u}_I \text{ along } \Gamma_I. \tag{3.1}$$

Boundary part	Transport	Flow
Inlet Γ_I	$c = c_I$ (fixed concentration)	$\vec{u} = \vec{u}_I = u_I \vec{e}_z$ (fixed profile)
Anode/MS Γ_A	$c = 0$ (infinitely fast reaction)	$\vec{u} = 0$ (no slip)
Outlet Γ_O	$\nabla c \cdot \vec{n} = 0$ (convective outflow)	$\nu(\nabla \vec{u})\vec{n} = p\vec{n}$
Symmetry Γ_S	$\nabla c \cdot \vec{n} = 0$ (symmetry)	$\vec{u} \cdot \vec{n} = 0, \nabla(\vec{u} \cdot \vec{t}) \cdot \vec{n} = 0$
Wall Γ_W	$\nabla c \cdot \vec{n} = 0$ (no flow)	$\vec{u} = 0$ (no slip)

TABLE 3.1. Boundary conditions for the flow cell.

In this fluid, a dissolved species with molar concentration $c \in H^1(\Omega)$ propagates according to the transport equation

$$\nabla \cdot (-D\nabla c + c\vec{u}) = \nabla \cdot \vec{q} = 0 \quad \text{and} \quad c = c_I \text{ along } \Gamma_I \tag{3.2}$$

for a given diffusion coefficient D and inlet concentration $c_I \in L^2(\Gamma_I)$. The quantity $\vec{q} := -D\nabla c + c\vec{u}$ is the molar flux of the species. Note, that the coupling assumes that the solution is dilute and ignores influences of the density changes on the fluid flow.

For the discussion in this paper, the computational domain Ω represents the void of the working chamber of a DEMS cell together with adjacent capillaries. Due to symmetry it reduces to the domain shown in Figure 2.1[right]. Further boundary conditions for the computational domain are listed in Table 3.1. Here, u_I denotes a Hagen–Poiseuille profile into the direction of the pipe $\vec{e}_z$ as inlet conditions for the velocity.

3.2. **Weak Formulation of the Stokes Equations.** The concept of weak solutions to the Stokes equations above is the basis for their discretisations by finite element methods and is briefly summarised here.

To derive the weak formulation, one can start from (3.1), multiply the first equations by some (smooth) velocity-related test vector field $\vec{v}$ with zero boundary data $\vec{v} = 0$ along all Dirichlet boundaries. Similarly, multiply the second equation by some (smooth) pressure-related test function q. Integration over the domain Ω and an integration by parts in the integrals on the left-hand side of the first equation result in

$$\int_\Omega \eta \nabla \vec{u} : \nabla \vec{v}\, dx - \int_\Omega (\nabla \cdot \vec{v}) p\, dx = \int_\Omega \vec{f} \cdot \vec{v}\, dx$$
$$\int_\Omega (\nabla \cdot \vec{u}) q\, dx = 0.$$

The boundary integrals from the integration by parts vanish due to the boundary conditions on $\vec{v}$ and $\vec{u}$. If $\vec{u}$ and p satisfy (3.1), these equations hold true for all test functions $\vec{v}$ and q. By density arguments and Sobolev space theory it suffices to test with $\vec{v} \in V := H_0^1(\Omega; \mathbb{R}^d)$, meaning $\vec{v} \in L^2(\Omega; \mathbb{R}^d), \nabla \vec{v} \in L^2(\Omega; \mathbb{R}^{d \times d})$ and zero boundary conditions along all Dirichlet boundaries. Similarly, it suffices to test only with $p \in Q := L_0^2(\Omega)$, meaning $p \in L^2(\Omega)$ and $\int_\Omega p\, dx = 0$.

With this, we call $\vec{u} \in H^1(\Omega; \mathbb{R}^d)$ and $p \in Q$ a weak solution of (3.1), if they satisfy

$$\int_\Omega \eta \nabla \vec{u} : \nabla \vec{v}\, dx - \int_\Omega (\nabla \cdot \vec{v}) p\, dx = \int_\Omega \vec{f} \cdot \vec{v}\, dx \quad \text{for all } \vec{v} \in V \tag{3.3}$$
$$\int_\Omega (\nabla \cdot \vec{u}) q\, dx = 0 \quad \text{for all } q \in Q.$$

Obviously, every solution of (3.1) is also a weak solution, while a weak solution needs further regularity to satisfy (3.1). Due to the Dirichlet boundary conditions, the semi-norm $\|\eta\nabla\bullet\|_{L^2(\Omega)}$ really is a norm in the space V, the so called energy norm, and renders $(V, \|\eta\nabla\bullet\|_{L^2(\Omega)})$ a Hilbert space, providing a straightforward way to set up discretization methods by regarding (3.3) in a finite dimensional subspace.

4. Numerical Discretisation

This section gives a brief description of the numerical discretisation. The basic idea to couple finite element methods for the fluid flow with a finite volume method for the species transport stems from [FLLB09, FLL11]. The main advantage of this coupling is the possibility to preserve mass conservation and the maximum principle for the concentration of transported species on the discrete level if the discrete solution for the velocity of the fluid flow is divergence-free. In [FLLB09, FLL11] this was ensured by using the Scott–Vogelius finite element method. However, this method is extremely expensive. Therefore, in the present paper, we give an update on novel techniques that restore the divergence-free property with drastically reduced computational costs.

4.1. Finite Element Methods for the Fluid Flow.

Finite element methods are based on the concept of weak solutions explained in Section 3.2 and replace the space of test functions in (3.3) by finite-dimensional subspaces of piecewise polynomials $V_h \subseteq V$ and $Q_h \subseteq Q$. This results in the search of some $\vec{u}_h \in V_h$ and $p_h \in Q_h$ such that

$$\begin{aligned} \int_\Omega \eta\nabla\vec{u}_h : \nabla\vec{v}_h \, dx - \int_\Omega (\nabla\cdot\vec{v}_h) p_h \, dx &= \int_\Omega \vec{f}\cdot\vec{v}_h \, dx \quad \text{for all } \vec{v}_h \in V_h \\ \int_\Omega (\nabla\cdot\vec{u}_h) q_h \, dx &= 0 \quad \text{for all } q_h \in Q_h. \end{aligned} \tag{4.1}$$

The discrete spaces of velocity ansatz functions V_h and pressure ansatz functions Q_h are formed by piecewise polynomials with respect to some regular triangulation $\mathcal{T}$ of Ω into triangles (in 2d) or tetrahedra (in 3d), such that the intersection of two different cells is either empty, or a single node, or a complete edge or a complete face (in 3d). The set of vertices is denoted by $\mathcal{N}$, and the set of faces is denoted by $\mathcal{F}$.

To ensure solvability of the discrete problem, an inf-sup condition has to be satisfied, which results in certain limitations in the choice of V_h and Q_h [GR86]. This often leads to the situation that the velocity test functions in the subspace

$$Z_h := \left\{ \vec{v} \in V \mid \int_\Omega (\nabla\cdot\vec{v}_h) q_h \, dx = 0 \text{ for all } q_h \in Q_h \right\}, \tag{4.2}$$

which is called the subspace of discretely divergence-free velocity test functions, are in general only approximately divergence-free. The use of discretely divergence-free test functions which are only approximately divergence-free has certain implications. One of them is a pressure-dependence in the a priori error estimate for the velocity in the energy norm

$$\|\nabla_h(\vec{u}-\vec{u}_h)\|_{L^2(\Omega)} \le C_1 \inf_{\vec{w}_h\in V_h} \|\nabla_h(\vec{u}-\vec{w}_h)\|_{L^2(\Omega)} + \frac{C_2}{\eta} \inf_{q_h\in Q_h} \|p-q_h\|_{L^2(\Omega)}. \tag{4.3}$$

If Z_h includes only divergence-free functions one can show that $C_2 = 0$ [LM14], while otherwise it holds $C_2 = 1$. If $C_2 = 1$, as it is the case for most of the currently used finite element formulations, and if the second term on the right-hand side is large compared to the first one, the discrete solution can develop severe spurious oscillations, even for very simple real-world situations [LM14]. Another implication which is important in the present context

is that a non divergence-free solution can lead to violations of the maximum principle in the coupled transport equation.

In this work we consider and compare five different finite element methods that are summarized in Table 4.1. The famous Taylor–Hood (TH) finite element method uses piecewise quadratic and continuous velocity ansatz functions and piecewise linear and continuous pressure ansatz functions. The Scott–Vogelius (SV) finite element method in $d = 3$ dimensions employs piecewise cubic and continuous velocity ansatz functions and piecewise quadratic discontinuous pressure ansatz functions. In 2D, the polynomial order of all ansatz functions can be reduced by one. However, the inf-sup stability can only be shown on certain barycentric refined triangulations $\mathcal{T}$ [Zha05, Qin94, AQ92]. The advantage of the Scott–Vogelius finite element method is that the discrete solution $\vec{u_h}$ of (4.1) is exactly divergence-free, while the solution of the Taylor–Hood method is in general only discretely divergence-free in the sense (4.2). The reason is that for the Scott–Vogelius method it holds $\nabla \cdot V_h \subseteq Q_h$, hence the second equation of (4.1) can be tested with $q_h = \nabla \cdot \vec{u_h}$, consequently $\nabla \cdot \vec{u_h} = 0$ holds exactly. This is also the reason for $C_2 = 1$ for the Taylor-Hood method and $C_2 = 0$ for the Scott-Vogelius method in (1.1).

Another popular method is known as the mini finite element method and employs piecewise linear velocity ansatz functions enriched by piecewise cell bubbles $\mathcal{B}(\mathcal{T})^d$ and piecewise linear continuous pressure ansatz functions. The set of cell bubbles $\mathcal{B}(\mathcal{T})$ consists of one polynomial b_T of order $d+1$ for each cell $T \in \mathcal{T}$ defined by the product of all nodal basis functions of the $d+1$ vertices $\mathcal{N}(T)$ of T, i.e.,

$$b_T = \prod_{z \in \mathcal{N}(T)} \varphi_z.$$

The nodal basis function φ_z of a node $z \in \mathcal{N}$ is a piecewise linear polynomial with $\varphi_z(z) = 1$ and $\varphi_z(y) = 0$ for all $y \in \mathcal{N} \setminus \{z\}$. Since the non-bubble basis polynomials of the mini finite element method have lowest order, also the convergence speed is lower than for the other methods. On the other hand, a higher convergence speed also needs higher smoothness of the exact solution which we do not expect in this application. Therefore, this method might still be competitive. Another lowest order method is the Bernardi–Raugel (BR) finite element method which enriches the piecewise linear velocity ansatz functions with normal-weighted face bubble functions, $b_F \vec{n}_F$ for all faces $F \in \mathcal{F}$, which allows a coupling with piecewise constant discontinuous pressure ansatz functions. The face bubble for a face $F \in \mathcal{F}$ is a polynomial of order d defined by the product of all those basis functions which correspond to the vertices $\mathcal{N}(F)$ that form the face, i.e.,

$$b_F := \prod_{z \in \mathcal{N}(F)} \varphi_z \quad \text{for each } F \in F.$$

The multiplication of each face bubble with the normal vector $\vec{n}_F$ (with an arbitrary but fixed orientation) of the face leads to the additional vector-valued ansatz functions for the Bernardi–Raugel finite element method.

Finally, we also consider the P2 bubble (P2B) finite element method where V_h consists of piecewise quadratic continuous ansatz functions plus the additional cell bubbles $\mathcal{B}(\mathcal{T})^d$ (and face bubbles in 3d). This allows to use piecewise linear and discontinuous pressure ansatz functions. Similarly to the case of the Taylor-Hood finite element, the solutions of the mini, Bernardi-Raugel and the P2 bubble finite element method are only discretely divergence-free in the sense of (4.2) but not exactly divergence-free.

Abbreviation	V_h	Q_h
BR	pcw. linear & cont. + normal-weighted face bubbles	pcw. constant
MINI	pcw. linear & cont. + cell bubbles	pcw. linear & cont.
TH	pcw. quadratic & cont.	pcw. linear & cont.
P2B	pcw. quadratic & cont. + cell bubbles (+ face bubbles in 3d)	pcw. linear
SV	pcw. quadratic (2d)/cubic (3d) & cont.	pcw. linear (2d)/quadratic (3d)

TABLE 4.1. List of finite element methods under consideration and their abbreviations.

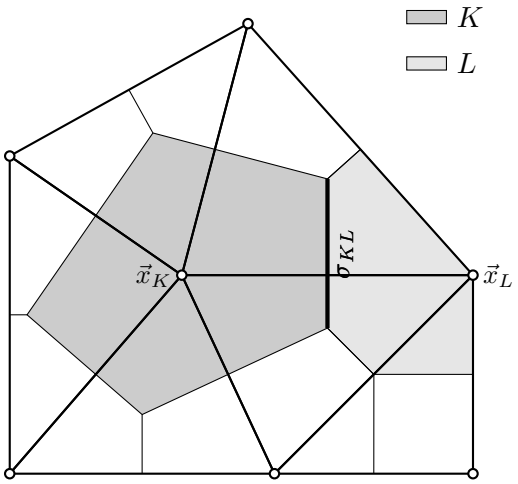

FIGURE 4.1. Two neighbouring Voronoi boxes K and L in the 2d finite volume method.

4.2. **Finite Volume Method for the Species Transport.** The finite volume method for the transport equation employs a partition $\mathcal{K}$ into Voronoi volumes based on a boundary conforming Delaunay triangulation [SGF10] of Ω. For every Voronoi box $K \in \mathcal{K}$, the divergence theorem yields

$$\int_K \nabla \cdot (-D\nabla c + c\vec{u})\, dx = \int_{\partial K} (-D\nabla c + c\vec{u}) \cdot \vec{n}\, ds$$

In order to couple the finite element discretization for the Stokes equations with the finite volume discretization of the advection-diffusion problem, we introduce a discrete velocity field $\vec{w}_h$. If the solution $\vec{u}_h$ of (4.1) is discretized with the Scott-Vogelius element, and thus exactly divergence-free, we set $\vec{w}_h := \vec{u}_h$. Otherwise, we set $\vec{w}_h := \widehat{\vec{u}}_h$, a divergence-free reconstruction of $\vec{u}_h$ defined in section 5.1. On every intersection of two Voronoi boxes $\sigma_{KL} := \partial K \cap \partial L$ as depicted in Figure 4.1 with $\tau_{\sigma_{KL}} := |\sigma_{KL}|/|\vec{x}_L - \vec{x}_K|$, we define a finite volume specific projection of the discrete velocity $\vec{w}_h$ by

$$w_{\sigma_{KL}} := \int_{\sigma_{KL}} \vec{w}_h \cdot (\vec{x}_L - \vec{x}_K)\, ds/|\sigma_{KL}|.$$

The flux approximation $g(c_K, c_L, w_{\sigma_{KL}}) := D\,(B(w_{\sigma_{KL}}/D)c_K - B(-w_{\sigma_{KL}}/D)c_L)$ between two cells with $B(z) = z/(1 - e^{-z}) > 0$ stems from an exponential fitting approximation of $(-D\nabla c + c\vec{u}) \cdot (\vec{x}_L - \vec{x}_K)$ [Il'69].

Eventually, the piecewise (with respect to $\mathcal{K}$) constant finite volume solution $c_h \in P_0(\mathcal{K})$ with $c_K := c_h|_K$ and $c_L := c_h|_L$ is characterised by the system of equations

$$\sum_{L \text{ neighbour of } K} \tau_{\sigma_{KL}}\; g(c_K, c_L, w_{\sigma_{KL}}) = 0 \quad \text{for all } K \in \mathcal{K}_0 := \mathcal{K} \setminus \mathcal{K}_D.$$

Details of this method and a convergence proof can be found in [FLL11]. The main advantage of this coupling is that it is capable of preserving the maximum principle for the concentration also on the discrete level if the discrete velocity $\vec{w}_h$ is exactly divergence-free. A proof for this can be found e.g. also in [FLL11]. This motivates the search for finite element methods or postprocessings that produce a divergence-free discrete velocity to achieve a mass-conservative coupling. The next section reports on novel recent approaches.

5. Mass Conservative Coupling

The section describes strategies how to attain a divergence-free approximate solution of the Navier-Stokes equations for a mass-conservative coupling in the transport equation.

5.1. **Global Divergence-Free Projection.** The idea here is to project the discrete velocity field $\vec{u}_h$ onto the divergence-free subspace of the Brezzi–Douglas–Marini (BDM) finite element space $BDM_k(\mathcal{T})$ of order k defined by

$$BDM_k(\mathcal{T}) := \left\{ \vec{r}_h \in P_k(\mathcal{T};\mathbb{R}^d) \,|\, \vec{r}_h \cdot \vec{n}_F \text{ is continuous on all faces } F \text{ of } \mathcal{T} \right\}.$$

The continuity condition of the normal flux on the faces ensures that every BDM function $\vec{r}_h$ has a divergence $\nabla \cdot \vec{r}_h \in L^2(\Omega)$. Then our projection is defined by the constrained best-approximation

$$\widehat{\vec{u}}_h = \operatorname*{argmin}_{\substack{\vec{r}_h \in BDM_k(\mathcal{T}),\\ \nabla\cdot\vec{r}_h = 0,\\ (\vec{r}_h - \vec{u}_h)\cdot\vec{n} = 0 \text{ along } \partial\Omega\setminus\Gamma_0}} \|\vec{r}_h - \vec{u}_h\|_{L^2(\Omega)}. \tag{5.1}$$

Note, that the normal component of the reconstruction matches exactly the normal component of the original discrete velocity along the boundary with Dirichlet or symmetry boundary conditions.

We choose $k = 1$ for the mini and Bernardi–Raugel finite element methods and $k = 2$ for the Taylor–Hood and P2 bubble finite element methods to match the degree of the velocity basis polynomials. The global reconstruction will be labeled with 'GR' below, e.g. 'BR+GR' denotes the Bernardi–Raugel finite element method with the described global a posteriori reconstruction of the discrete solution.

5.2. **Pressure-Robust Finite Element Methods.** The P2 bubble finite element method and the Bernardi-Raugel finite element method can be modified such that the pressure-dependence in the a priori error estimate vanishes, i.e. it holds $C_2 = 0$ in (1.1). The idea behind this is based on [Lin14] and summarizes as follows: the discrete equations have to be tested with divergence-free test functions (while trial functions remain unchanged). To do so we employ the $BDM_1(\mathcal{T})$ standard interpolation in case of the Bernardi–Raugel finite element method and the $BDM_2(\mathcal{T})$ standard interpolation in case of the P2 bubble finite element method. Details on the interpolation and its properties can be found in the textbook [BF91]. This BDM interpolation operator Π_{BDM} is exact, i.e. $\Pi_{\text{BDM}}\vec{v}_h = \vec{v}_h$ when applied to a piecewise linear (for $k = 1$) or quadratic (for $k = 2$) continuous velocity ansatz function v_h, hence only the bubble basis functions are modified by the interpolation. The main property for the reconstruction of vector-valued cell bubbles $\vec{b}_T$ and face bubbles $\vec{b}_F$ is that

$$\int_T q\nabla\cdot(\Pi_{\text{BDM}}\vec{b}_T)\,dx = \int_T q\vec{b}_T\,dx \quad \text{for all } q \in P_1(T),$$
$$\int_T q\nabla\cdot(\Pi_{\text{BDM}}\vec{b}_F)\,dx = \int_T q\vec{b}_F\,dx \quad \text{for all } q \in P_0(T).$$

Given the P2 bubble finite element solution $\vec{u}_h = \vec{u}_2 + \vec{u}_b$ with the cell bubble part $\vec{u}_b := \sum_{T\in\mathcal{T}} \alpha_T b_T$ and the piecewise quadratic remainder $\vec{u}_2$, the application of the $BDM_2(\mathcal{T})$ interpolation leads to the piecewise quadratic function

$$\Pi_{\mathrm{BDM}}\vec{u}_h = \vec{u}_1 + \sum_{T\in\mathcal{T}} \alpha_T \Pi_{\mathrm{BDM}}\vec{b}_T \in P_2(\mathcal{T}).$$

Since $\vec{u}_h$ is a discretely divergence-free function in the sense of (4.2), the properties above imply that its BDM interpolation $\Pi_{\mathrm{BDM}}\vec{u}_h$ is exactly divergence-free. Hence, the local interpolation of the bubbles lead to a global reconstruction operator that maps discretely divergence-free functions onto divergence-free ones. The same holds for the Bernardi–Raugel finite element method and the $BDM_1(\mathcal{T})$ interpolation. Also note that, due to the boundary conditions of the bubble, its BDM interpolation is very local and therefore quite easy to implement. In fact, the support of the reconstructed bubble is the same as the support of the bubble itself. This makes the global reconstruction less costly than the best-approximation (5.1), but of course, also less optimal. To distinguish the two operators in the comparisons below, the one based on the local bubble reconstructions is denoted with the label 'LR'.

The local interpolations are also used to modify the discrete system of equations in the right-hand side, i.e.,

$$\begin{aligned} \int_\Omega \eta\nabla\vec{v}_h : \nabla\vec{u}_h\,dx - \int_\Omega (\nabla\cdot\vec{v}_h)p_h\,dx &= \int_\Omega \vec{f}\cdot(\Pi_{\mathrm{BDM}}\vec{v}_h)\,dx \quad \text{for all } \vec{v}_h \in V_h \\ \int_\Omega (\nabla\cdot\vec{u}_h)q_h\,dx &= 0 \quad \text{for all } q_h \in Q_h. \end{aligned} \tag{5.2}$$

The application of the reconstruction operator in the right-hand side ensures that the first equation is tested with exactly divergence-free functions and not only with discretely divergence-free functions. This improves the a priori error estimates by removing the pressure-dependence therein, i.e. $C_2 = 0$ in (1.1). Details can be found in [Lin14, LMT15]. Note, that the use of the BDM interpolation is a slight difference compared to the modifications suggested in [LMT15], but has the two advantages that, first, only the bubble functions have to be modified and that, second, the BDM interpolation operator is more accurate than the Raviart–Thomas based interpolation suggested in [LMT15].

5.3. **Special Situation for $\vec{f} = 0$.** If the right-hand side $\vec{f}$ of the Stokes equations vanishes as in the examples below, the discrete solutions of the pressure-robust finite element methods of Section 5.2 equals the discrete solutions of their unmodified parent methods. This is the case for the experiments below and results in a comparison of just different globally and locally constructed divergence-free projection operators. Please note, that for more involved models with $\vec{f} \neq 0$ or additional nonlinear convection or Coriolis force terms divergence-free test functions play a role and lead to significant improvements in the quality of the discrete solution [LM14]. In the present application, the nonlinear convection term $(\vec{u}\cdot\nabla)\vec{u}$ is small und was removed from the model for simplicity.

6. Fitting Procedure

This section summarizes the experimental work flow and how the data was used to determine the unknowns in the model, namely the inlet concentration C_I, the diffusion coefficient D and the working chamber height H.

lvl	BR	MINI	TH	P2B	SV
1	2.195	2.196	2.890	5.422	12.334
2	9.123	9.124	11.874	22.988	52.964
3	38.063	38.064	49.238	96.900	224.700
4	153.435	153.436	197.882	392.568	913.152
5	616.019	616.020	793.250	1.580.064	3.681.096

TABLE 7.1. Number of degrees of freedom (ndof) for different refinement levels for the 2D experiment.

6.1. **Experiment.** The first step is the calibration of the system, i.e. the detection of the relation between mass flow and measured mass spectrometric current for oxygen molecules. This is done in a separate experiment shortly before and after the main experiments. Details of the calibration process can be found in [Kho15, BFKM15].

In the main experiments the mass spectrometric currents of oxygen were recorded for ten distinct flow rates in the range of 0.1 to $80\mu l.s^{-1}$ and for several O_2 saturated solvents that flow through the dual thin-layer flow cell. Due to water evaporation through the pores of the hydrophobic Teflon membrane the flow rates were corrected by extrapolation of the data in the low flowrate regime. Details of this correction can be found in [BFKM15].

Finally, the output of the experiments are data pairs of the form u_j, I_j, $j = 1, \dots, 10$ were u_j is the corrected flow rate and I_j is the recorded current for the O_2 molecules.

6.2. **Interpretation.** The range of flowrates were chosen such that transport of the solute molecules for the lowest flow rate can be assumed strongly diffusion-dominated while for the highest flow rate the transport is convection-dominated. This allows to calculate the unknown inlet concentration from the first measurement, since (almost) all O_2 molecules are consumed at the teflon membrane leading to the mass spectrometer. This assumption was also verified by the simulations, were the concentration at the outlet decreased by more than 99%.

With the inlet concentration and literature data for the viscosity and density of the solvent, the system of partial differential equations was solved for an initial guess for the diffusion coefficient D. Then, D was fitted using the Levenberg-Marquardt algorithm [MGH80] with square mean of the difference between measured and simulated membrane fluxes for the different flow rates as the least squares input function.

However, due to the experimental construction, the working chamber height H is not known precisely and only known to be in the range $H \in (50\mu m, 100\mu m)$. To fix this height, the described procedure was repeated for different computational domains with different working chamber height for the well-studied solvent O_2 saturated water [HB96]. For each choice of H different fitted diffusion coefficients were calculated. Then, the height was chosen that produces the diffusion coefficient that is closest to the literature data [HB96]. This resulted in $H = 70\mu m$, a value close to the intended one, and fixed the working chamber heights for the remaining simulations with the other solvents.

7. Numerical Experiments and Discussion

This section shows the result of some numerical experiments to verify the convergence of the implemented methods and the fitting results with real experimental data.

7.1. **2D Simulation with Virtual Data.** To test the numerical methods and their convergence within the fitting procedure, virtual measurement data u_j, I_j, $j = 1, \dots, 10$, for the inlet concentration $c_I = 1 mmol/dm^3$ and the diffusion coefficient $D = 1 \cdot 10^{-9} m^2/s$ were created by a calculation on refinement level 6 of the two-dimensional domain depicted in Figure 7.1 with the Scott–Vogelius finite element method. The dimension and the boundary

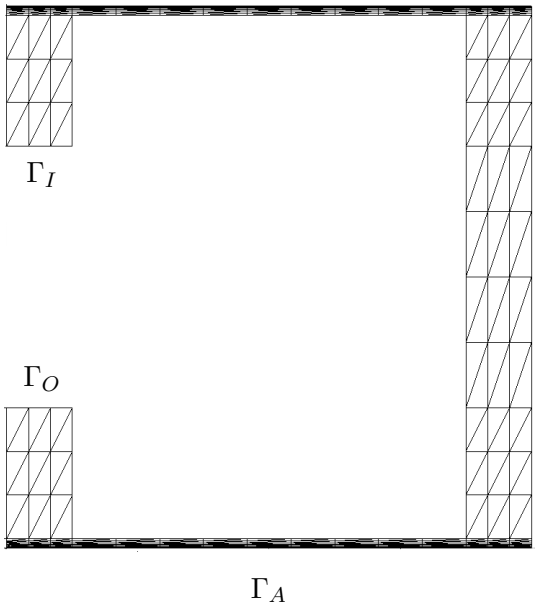

FIGURE 7.1. Initial mesh (lvl=1) for the 2d experiment with virtual data, essentially corresponding to a 2D cut through a full DEMS cell with two working chambers. Indicated are the inlet Γ_I, the outlet Γ_O and the interface to the mass spectrometric compartment Γ_A. All other boundary segments belong to the inert boundary Γ_W.

conditions of the domain were chosen similarly to that of a vertical cut through the real flow cell from Figure 2.1. The calculated currents where used as surrogate measurements and fed into the fitting procedure described in section 6.2.

Table 7.2 displays the fitted diffusion coefficient for different refinement levels for all finite element methods under consideration. All methods converge to the correct value, but the convergence for the Bernardi–Raugel element seems a bit slower.

Table 7.3 shows the maximal concentrations, which by the maximum principle should not exceed the inlet concentration. While the Taylor–Hood, the Bernardi–Raugel, the mini and the P2 bubble finite element method show violations of the maximum principle, as expected by theory, the Scott–Vogelius finite element method and all methods with reconstruction (+GR or +LR) do not violate the maximum principle. Among the non divergence-free methods the P2 bubble finite element method is the one with the smallest violation and it is also the method with the best results on the coarsest refinement level.

However, the quality of the fit of the diffusion coefficient does not seem to be affected strongly by this violation as the results with and without reconstruction are very similar at least on the higher refinement levels. Only the Bernardi–Raugel finite element method shows large differences, especially on the coarser refinement levels where the unmodified method does not converge at all (or to negative diffusion coefficients marked by '-') while the modified method converges notably faster to the exact value.

The difference between global (+GR) and local reconstruction (+LR) is significant on the coarser refinement but vanishes on higher refinement levels. As a conclusion, it seems appropriate to use the more expensive global divergence-free projection on the coarser refinement levels.

In the competition between the equally expensive mini finite element method and the Bernardi–Raugel finite element method, the mini finite element method seems to deliver more accurate fitted diffusion coefficients. However, the Bernardi–Raugel finite element method

					$D/10^{-9}m^2/s$						
lvl	BR	BR+GR	BR+LR	MINI	MINI+GR	TH	TH+GR	P2B	P2B+GR	P2B+LR	SV
1	-	0.630	-	0.735	0.705	-	0.740	0.925	0.836	0.791	0.786
2	-	0.826	0.691	0.989	0.892	0.921	0.910	0.953	0.936	0.933	0.930
3	0.727	0.946	0.926	1.017	0.961	0.977	0.966	0.972	0.968	0.970	0.969
4	0.897	0.980	0.981	1.003	0.982	0.987	0.985	0.985	0.984	0.984	0.984
5	0.961	0.990	0.990	0.997	0.990	0.991	0.991	0.990	0.990	0.990	0.990
6											1.000

TABLE 7.2. Diffusion coefficients D for different refinement levels and different finite element methods for the 2d experiment with virtual data in Section 7.1.

					$\max c/\, mol\, m^{-3}$						
lvl	BR	BR+GR	BR+LR	MINI	MINI+GR	TH	TH+GR	P2B	P2B+GR	P2B+LR	SV
1	-	1.000	1.000	2.291	1.000	-	1.000	1.251	1.000	1.000	1.000
2	-	1.000	1.000	2.032	1.000	2.507	1.000	1.273	1.000	1.000	1.000
3	14.22	1.000	1.000	2.355	1.000	2.363	1.000	1.254	1.000	1.000	1.000
4	4.578	1.000	1.000	2.596	1.000	2.324	1.000	1.224	1.000	1.000	1.000
5	4.336	1.000	1.000	2.827	1.000	2.772	1.000	1.180	1.000	1.000	1.000

TABLE 7.3. Maximal concentration for different refinement levels and different finite element methods for the 2d experiment with virtual data in Section 7.1.

offers an easy implementation of the local reconstruction, while a local reconstruction for the mini finite element method is still under investigation but is certainly more involved as the continuous pressure leads to larger local problems that have to be solved.

7.2. **Full DEMS Cell Simulation.** This section reports on the results from the fitting procedure described in Section 6 and compares the results with the conclusions from the experiments [Kho15] and literature data. Here, only the results of the Taylor–Hood finite element method on very fine meshes with about 2.5 million degrees of freedom are displayed. Computations with the Scott–Vogelius and mini finite element methods led to very similar results. The suggested methods with divergence-free reconstructions are not yet fully implemented in 3D. However, we expect a similar behaviour as in the 2D experiment and no significant differences between all methods in terms of the diffusion coefficient on the finest mesh. In terms of computational costs the locally reconstructed Bernardi-Raugel and the globally reconstructed mini finite element method are highly attractive. However, for the present application the widely used Taylor-Hood finite element method seems sufficient.

Figure 7.2 shows the fitted diffusion coefficients for different solvents in dependence of the unknown working chamber height H. With the fixed height of $H = 70\mu m$ the diffusion coefficients read

$$D_{O_2/\text{0.1M KOH}} = 2.14 \cdot 10^{-9} m^2/s \qquad D_{O_2/\text{0.1M LiOH}} = 2.14 \cdot 10^{-9} m^2/s$$
$$D_{O_2/\text{1.0M KOH}} = 2.07 \cdot 10^{-9} m^2/s \qquad D_{O_2/\text{PC}} = 1.70 \cdot 10^{-9} m^2/s$$
$$D_{O_2/\text{2.5M KOH}} = 1.75 \cdot 10^{-9} m^2/s \qquad D_{O_2/\text{DMSO}} = 1.47 \cdot 10^{-9} m^2/s$$

Qualitatively, the values show that the diffusion coefficient decreases with an increasing concentration of salt in the solvent, which is known under the "salting out" effect. Quantitatively, the values are also close to literature values in cases where they are available.

8. Beyond limiting current measurements

This section gives an outlook for a possible extension of the model to include surface reactions and the option to determine reaction constants by fitting to cyclic voltammetry (CV) measurements, which is planned to be exploited in forthcoming research.

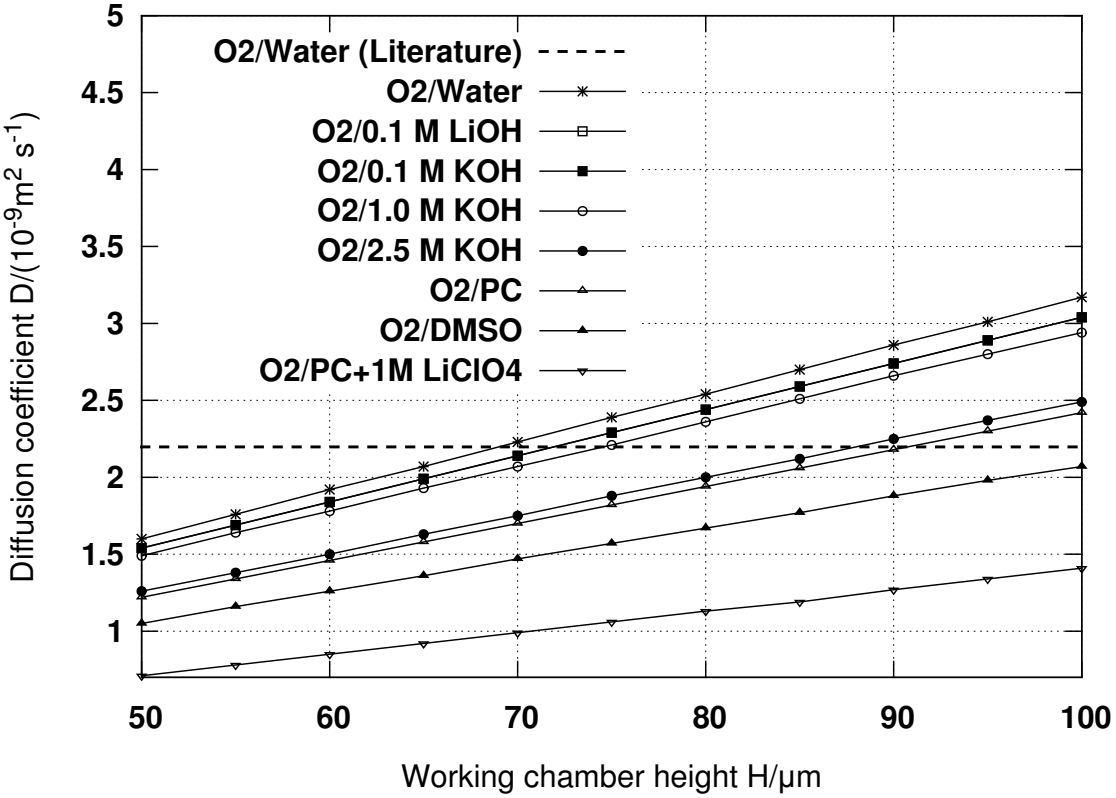

FIGURE 7.2. Diffusion coefficients D for different solvents in dependence of the unknown working chamber height H.

We consider a simple redox reaction

$$O + ne^- \underset{\text{ox}}{\overset{\text{red}}{\rightleftharpoons}} R.$$

In order to be able to simulate the complete CV experiment, two time dependent convective diffusion equations in a stationary flow have to be solved simultaneously:

$$\partial_t c_O + \nabla \cdot (-D_O \nabla c_O + c_O \vec{u}) = 0 \tag{8.1}$$

$$\partial_t c_R + \nabla \cdot (-D_R \nabla c_R + c_R \vec{u}) = 0 \tag{8.2}$$

With the exception of the working electrode Γ_A, all boundary conditions are similar to those listed in table 3.1. Under the postulate of diluteness, the assumption of a stationary flow regime is kept unchanged.

For a given value σ of the electrical conductivity, the electrostatic potential ϕ in the cell follows Ohm's law

$$\nabla \cdot \sigma \nabla \phi = 0 \tag{8.3}$$

with a prescribed time dependent potential $\phi = \phi_{CE}(t)$ at the counter electrode placed at the outlet boundary Γ_O of the cell.

The boundary condition at the working electrode employs the Butler-Volmer rate equation

$$\frac{j}{nF} = k^+ c_O \exp\left(-\alpha n F \frac{\Delta\phi}{RT}\right) - k^- c_R \exp\left((1-\alpha) n F \frac{\Delta\phi}{RT}\right), \tag{8.4}$$

where $\Delta\phi = \phi - \phi_{WE}$ is the difference between the electrolyte potential and the fixed applied potential ϕ_{WE} at the working electrode. In the absence of double layer effects, the boundary conditions at the working electrode read as follows:

$$\nabla \cdot (-D_O \nabla c_O + c_O \vec{u}) \cdot \vec{n} = -\frac{j}{nF} \tag{8.5}$$

$$\nabla \cdot (-D_R \nabla c_R + c_R \vec{u}) \cdot \vec{n} = \frac{j}{nF} \tag{8.6}$$

$$-\sigma \nabla \phi \cdot \vec{n} = j. \tag{8.7}$$

The resulting system of partial differential equations is now time dependent and nonlinear. We choose the unconditionally stable backward Euler method for discretization in time, which guarantees the absence of nonphysical oscillations of the discrete solution. As a result, for each time step, a nonlinearily coupled problem for the transported species and the electrostatic potential is solved by Newton's nonlinear iteration method. Due to stationarity of the flow regime, the Navier-Stokes equations need to be solved only once for the whole time dependent process.

The solution process described so far allows to simulate a two-electrode setup: calculate the Faradaic current

$$I(t) = \int_{\Gamma_A} j \, ds \tag{8.8}$$

from the solution $(c_O(t), c_R(t), \phi(t))$ given by the system (8.1)-(8.3) with controlled potential at the counter electrode $\phi_{CE}(t)$.

In order to match the three-electrode setup commonly used electrochemical experiments, this procedure needs to be enhanced to take into account the potentiostatic control of the potential at the reference electrode. A straightforward model for an reference electrode is based on the choice of a placement point in the interior of the cell. For the the DEMS experiment it is placed close to the inlet. Assuming the ideal case of infinite resistance of the reference electrode, the model of the measurement of the electrostatic potential at the reference electrode simply consists in the evaluation of the electrostatic potential ϕ_{RE} in the given point. Being dependent on the applied potential ϕ_{CE} at the counter electrode, in each timestep it can be considered as a function

$$\phi_{RE} = \phi_{RE}(\phi_{CE}), \tag{8.9}$$

where one evaluation of this function consists in one solution of the time discrete system (8.1)-(8.3) at a given moment of time. Demanding

$$\phi_{RE}(\phi_{CE}) = \phi_{CV}(t) \tag{8.10}$$

where $\phi_{CV}(t)$ typically is the prescribed sawtooth profile for potentiostatic measurements. This procedure provides a model for the standard three-electrode setup which is able to take into account the uncompensated resistance [BF80] between working electrode and reference electrode, and the fact that the potential at the electrolyte side of the working electrode generally depends on the location on the electrode surface.

Equation (8.10) is again nonlinear, therefore its solution adds an additional iteration layer per time step on top of the Newton iteration to solve (8.1)-(8.3). Due to the difficulty of establishing the derivative $\phi'_{RE}(\phi_{CE})$, a derivative-free method is the best choice here. While the secant method works well for this case, our choice is the Broyden hypersecant method [CC09], which is slightly more economical and works as well for multiple variables.

In order to demonstrate the possibilities opened up by this procedure, we provide the results of a synthetic cyclic voltammogram (CV) experiment. Choosing $k^+ = k^- = 1.0 \cdot$

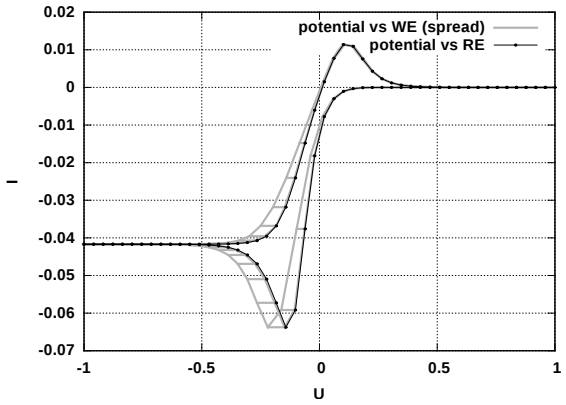

FIGURE 8.1. Cyclic voltammogram of a redox reaction with synthetic data. Black: I vs. $\phi_{WE}^{\text{metal}} - \phi_{RE}$. Grey: I vs. $\phi_{WE}^{\text{metal}} - \phi_{WE}^{\text{solution}}$, exhibiting the range of potential values assumed at the electrolyte side of the working electrode.

$10^{-5}m/s$, $D_O = D_R = 3.9 \cdot 10^{-9}m^3/s$, $\sigma = 10^{-2}S/cm$, $c_{O,in} = 5 \cdot 10^{-4}mol/dm^3, c_{R,in} = 0$, one CV sweep corresponding to a sweep rate of $100mV/s$ for the reference electrode potential is calculated in the geometry of the 3D dems cell (fig. 2.1). The resulting Faradaic current values are randomly perturbed with an error margin of 2.5% in order to provide the synthetic measurement data. Then, a fit procedure based on the Levenberg Marquardt method [MGH80] is used to establish those values of k^+, k^- which result in the best least squares fit of the corresponding CV data to the synthetic measurement data. As a result, after 22 fitting steps, estimated values of $k^+ = 9.82 \cdot 10^{-6}m/s, k^- = 9.73 \cdot 10^{-6}m/s$ are obtained.

Figure 8.1 plots two variants of the resulting CV. The black curve shows the electrode current I vs. the difference between the potential applied at the working electrode ϕ_{WE}^{metal} and the value at the reference electrode ϕ_{RE}. The grey curves plot the current I vs. the difference between the potential applied at the working electrode ϕ_{WE}^{metal} and the value $\phi_{WE}^{\text{solution}}$ occurring at the electrolyte side of the working electrode. As already remarked, this value depends on the location on the electrode surface, therefore for a given bias, its minimum and maximum values along with a horizontal bar joining them is plotted in order to indicate the value spread of this potential. The origin of this spread is the inhomogeneous iR drop within the thin layer, and, related to that, the somewhat different current density at the center and at outer parts of the working electrode.

The procedure described above will be used in future for fitting true experimental data.

Acknowledgments. The research documented in this paper has been partially funded in the framework of the project "Macroscopic Modeling of Transport and Reaction Processes in Magnesium-Air-Batteries" (Grant 03EK3027D) under the research initiative "Energy storage" of the German Federal government.

REFERENCES

[ACF+11] Matthias Augustin, Alfonso Caiazzo, André Fiebach, Jürgen Fuhrmann, Volker John, Alexander Linke, and Rudolf Umla, *An assessment of discretizations for convection-dominated convection–diffusion equations*, Computer Methods in Applied Mechanics and Engineering **200** (2011), no. 47, 3395–3409.

[AES14] B. J. Adesokan, A. Evgrafov, and M. P. Sørensen, *Simulating cyclic voltammetry under advection for electrochemical cantilevers*, Mathematical Methods in the Applied Sciences (2014), doi=10.1002/mma.3336.

[AKS10] Christian Amatore, Oleksiy Klymenko, and Irina Svir, *A new strategy for simulation of electrochemical mechanisms involving acute reaction fronts in solution: Principle*, Electrochemistry Communications **12** (2010), no. 9, 1170–1173.

[AQ92] Douglas N. Arnold and Jinshui Qin, *Quadratic velocity/linear pressure Stokes elements*, Advances in Computer Methods for Partial Differential Equations VII (R. Vichnevetsky, D. Knight, and G. Richter, eds.), IMACS, 1992, pp. 28–34.

[Bal04] Helmut Baltruschat, *Differential electrochemical mass spectrometry*, Journal of the American Society for Mass Spectrometry **15** (2004), no. 12, 1693–1706.

[BF80] Allen J Bard and Larry R Faulkner, *Electrochemical methods: fundamentals and applications*, vol. 2, Wiley New York, 1980.

[BF91] Franco Brezzi and Michel Fortin, *Mixed and hybrid finite element methods*, Springer-Verlag New York, Inc., New York, NY, USA, 1991.

[BFKM15] H. Baltruschat, J. Fuhrmann, M. Khodayari, and C. Merdon, *A new method for determination of solubility and diffusion coefficient of gases in aqeueous and non-aqueous electrolytes: application to oxygen (submitted)*.

[CC09] Johan Carlsson and John R Cary, *The hypersecant jacobian approximation for quasi-newton solves of sparse nonlinear systems*, arXiv preprint arXiv:0905.1054 (2009).

[CLW14] R. G. Compton, E. Laborda, and K. R. Ward, *Understanding voltammetry - simulation of electrode processes*, World Scientific, 2014.

[FLL11] J. Fuhrmann, A. Linke, and H. Langmach, *A numerical method for mass conservative coupling between fluid flow and solute transport*, Appl. Num. Math. **61** (2011), no. 4, 530 – 553.

[FLLB09] J. Fuhrmann, A. Linke, H. Langmach, and H. Baltruschat, *Numerical calculation of the limiting current for a cylindrical thin layer flow cell*, Electrochimica Acta **55** (2009), 430–438.

[FZH+08] Jürgen Fuhrmann, Hong Zhao, Ekkehard Holzbecher, Hartmut Langmach, Malgorzata Chojak, Rune Halseid, Zenonas Jusys, and J Behm, *Experimental and numerical model study of the limiting current in a channel flow cell with a circular electrode*, Physical Chemistry Chemical Physics **10** (2008), no. 25, 3784–3795.

[GR86] V. Girault and P.-A. Raviart, *Finite element methods for Navier-Stokes equations*, Springer Series in Computational Mathematics, vol. 5, Springer-Verlag, Berlin, 1986.

[HB96] P. Han and David M. Bartels, *Temperature dependence of oxygen diffusion in H2O and D2O*, J. Phys. Chem. **100** (1996), 5597–5602.

[Il'69] A. M. Il'in, *A difference scheme for a differential equation with a small parameter multiplying the second derivative*, Mat. zametki **6** (1969), 237–248.

[JK07] Volker John and Petr Knobloch, *On spurious oscillations at layers diminishing (sold) methods for convection–diffusion equations: Part i–a review*, Computer Methods in Applied Mechanics and Engineering **196** (2007), no. 17, 2197–2215.

[JMB99] Z Jusys, H Massong, and H Baltruschat, *A new approach for simultaneous dems and eqcm: Electro-oxidation of adsorbed co on pt and pt-ru*, Journal of the electrochemical Society **146** (1999), no. 3, 1093–1098.

[Kho15] M. Khodayari, *characterization of dual thin-layer flow through cell and determination of solubility and diffusion coefficient of oxygen in aqueous and non-aqueous electrolytes*, Ph.D. thesis, 2015.

[Lev62] Veniamin G Levich, *Physicochemical hydrodynamics*, vol. 689, Prentice-hall Englewood Cliffs, NJ, 1962.

[Lin14] Alexander Linke, *On the role of the Helmholtz decomposition in mixed methods for incompressible flows and a new variational crime*, Comp. Methods Appl. Mech. Engrg. **268** (2014), 782–800.

[LM14] A. Linke and C. Merdon, *On spurious oscillations due to irrotational forces in the Navier–Stokes momentum balance*, WIAS Preprint (2014), no. 2132.

[LMT15] Alexander Linke, Gunar Matthies, and Lutz Tobiska, *Robust arbitrary order mixed finite element methods for the incompressible stokes equations with pressure independent velocity errors*, ESAIM: M2AN (2015).

[MGH80] Jorge J Moré, Burton S Garbow, and Kenneth E Hillstrom, *User guide for minpack-1*, Tech. report, CM-P00068642, 1980.

[NTA12] John Newman and Karen E Thomas-Alyea, *Electrochemical systems*, John Wiley & Sons, 2012.

[Qin94] J. Qin, *On the convergence of some low order mixed finite elements for incompressible fluids*, Ph.D. thesis, Pennsylvania State University, 1994.

[SGF10] Hang Si, K Gärtner, and J Fuhrmann, *Boundary conforming delaunay mesh generation*, Computational Mathematics and Mathematical Physics **50** (2010), no. 1, 38–53.

[Zha05] S. Zhang, *A new family of stable mixed finite elements for the 3d Stokes equations*, Math. Comp. **74** (2005), no. 250, 543–554.